


Quenched disorder and instability control dynamic fracture in three dimensions

Received: 14 February 2024

Accepted: 6 August 2024

Published online: 29 August 2024

 Check for updatesYuri Lubomirsky¹ & Eran Bouchbinder¹ 

Materials failure in 3D still poses basic challenges. We study 3D brittle crack dynamics using a phase-field approach, where Gaussian quenched disorder in the fracture energy is incorporated. Disorder is characterized by a correlation length R and strength σ . We find that the mean crack velocity v is bounded by a limiting velocity, which is smaller than the homogeneous material's prediction and decreases with σ . It emerges from a dynamic renormalization of the fracture energy with increasing crack driving force G , resembling a critical point, due to an interplay between a 2D branching instability and disorder. At small G , the probability of localized branching on a scale R is super-exponentially small. With increasing G , this probability quickly increases, leading to misty fracture surfaces, yet the associated extra dissipation remains small. As G is further increased, branching-related lengthscales become dynamic and persistently increase, leading to hackle-like structures and a macroscopic contribution to the fracture surface. The latter dynamically renormalizes the actual fracture energy until, eventually, any increase in G is balanced by extra fracture surface, with no accompanying increase in v . Finally, branching width reaches the system's thickness such that 2D symmetry is statistically restored. Our findings are consistent with a broad range of experimental observations.

Materials failure is a physical phenomenon of prime scientific and technological importance, which continues to pose fundamental challenges^{1–5}. It is mediated by the propagation of cracks, which are dynamic defects that feature extreme conditions near their edges – mimicking a mathematical singularity – and accelerate to relativistic velocities (relative to elastic wave speeds) in brittle materials^{6,7}. Moreover, crack dynamics involve strongly non-equilibrium physics, long-range elastodynamic interactions and a wide range of spatio-temporal scales, which still resist a complete theoretical understanding.

Things somewhat simplify in 2D, i.e., when experiments in thin samples are considered^{8,9}, where a crack is the trajectory left behind a propagating tip (a point). Major progress in understanding rapid crack dynamics in 2D has been recently made^{9–13}. In particular, high-velocity symmetry-breaking instabilities have been predicted, in quantitative agreement with experiments, including the 2D oscillatory instability⁸

and the 2D branching instability (sometimes also termed macro-branching/tip-splitting)⁹. These two instabilities are linear instabilities, which are spontaneously triggered by infinitesimal noise, once the critical conditions are met.

Our corresponding understanding of dynamic fracture in 3D lags far behind. In 3D, the sample thickness is no longer a negligible dimension, and a crack is the surface left behind a propagating line, i.e., here, the crack edge is a 2D front, see Fig. 1a. While available experiments on brittle amorphous materials shed important light on the phenomenology of dynamic fracture in 3D^{14–29}, our fundamental understanding of the underlying physics remains limited. These experiments revealed a variety of 3D out-of-plane crack structures, including micro-cracking damage^{14–17}, surface steps^{18,19}, cross-hatching patterns²⁰, micro-branches^{21–24,30} and mirror-mist-hackle patterns^{25–27,29}, all emerging at mean crack front velocities smaller than the 2D instability thresholds.

¹Chemical and Biological Physics Department, Weizmann Institute of Science, Rehovot 7610001, Israel. ✉ e-mail: eran.bouchbinder@weizmann.ac.il

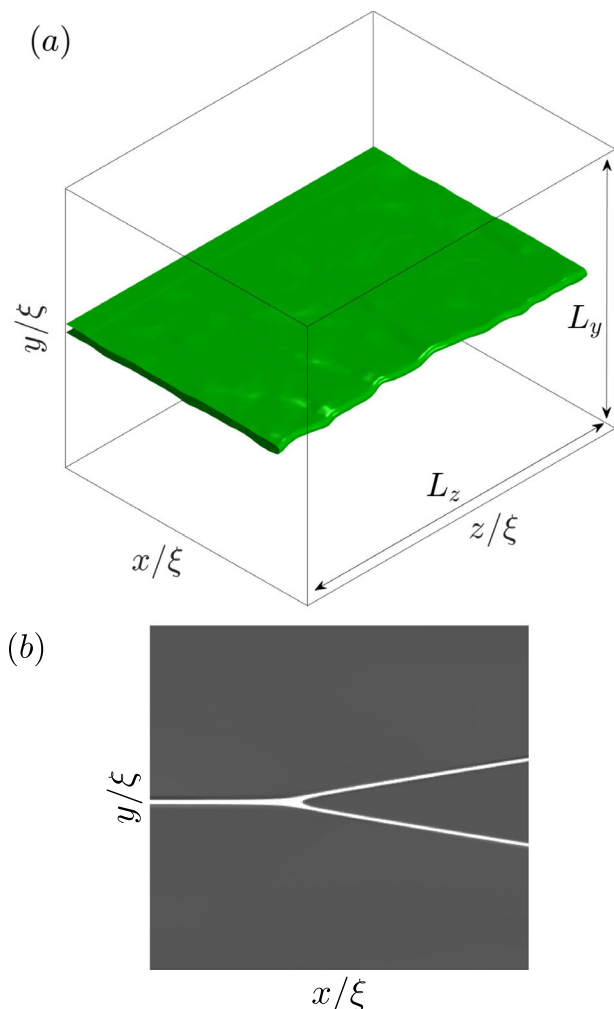


Fig. 1 | Crack propagation in 3D and the linear 2D branching instability. **a** A sketch of a 3D tensile crack experiment in a long bar of height L_y and thickness L_z . The long bar features a length $L_x \gg L_y, L_z$, and only a small section of it is shown. The crack is located in the middle (symmetry) plane and will subsequently propagate predominantly in the x direction in response to a sufficiently large crack driving force G (related to the tensile loading, applied in the y direction). We employ periodic boundary conditions along the z direction (see “Methods”). The coordinates are normalized by the dissipation length ξ , see text for definition. **b** A linear crack branching instability in 2D, i.e., $L_z = 0$, occurring at a very high propagation velocity $v_B = 0.95c_R$ (c_R is the Rayleigh wave-speed), once a threshold tensile driving force G_B is surpassed. See text and Fig. 2 for additional discussion.

Here, we study 3D dynamic fracture using a flexible computational framework in which material quenched disorder is incorporated. It is based on a phase-field fracture approach^{9,12,13,31–36}, which is particularly suitable for studying 3D dynamic fracture as it allows cracks to self-consistently select complex 3D trajectories (including topological changes) without imposing any external path selection criteria. Moreover, it allows to track the in silico real-time 3D spatiotemporal dynamics of cracks in a way that goes well beyond current experiments. This framework quantitatively predicted the 2D high-velocity oscillatory and branching instabilities in homogeneous materials^{9,12,13}, as well as the dynamics of crack front waves in 3D homogeneous materials with isolated heterogeneities³⁴.

Evidence regarding 3D dynamic fracture is largely obtained in experiments on amorphous materials, such as various glassy polymers^{14–17,21–23,29}, silica glasses^{22,25–28} and brittle elastomers²⁴. These materials are intrinsically disordered, featuring fluctuations in material properties over various lengthscales. Material disorder and

heterogeneity have been extensively discussed, mainly in the context of in-plane fracture roughness in 3D and mostly in the quasi-static regime^{3,37}. Some recent studies considered the effect of material heterogeneity on dynamic in-plane cracks³⁸ and on quasi-static out-of-plane cracks³⁹. Yet, the interaction of a 3D elastodynamic crack with continuous quenched disorder has not been studied theoretically. We show that the interplay between quenched disorder and the 2D branching instability controls dynamic fracture in 3D, in agreement with a wide range of experimental observations.

Results

Dimensionality, stability and disorder-induced limiting velocity

A canonical experiment for probing failure dynamics involves an initial planar crack located in the middle plane of a long 3D rectangular bar, see Fig. 1a. The bar features height L_y , thickness L_z and length $L_x \gg L_y, L_z$, where the (x, y, z) coordinate system is defined in Fig. 1. It is loaded symmetrically by small tensile displacements $u_y(x, y = \pm L_y/2, z, t) = \pm \delta/2$, where $\mathbf{u}(x, y, z, t)$ is the 3D displacement field and t is time. The tensile loading corresponds to a crack driving force $G = E\delta^2/L_y$ (the linear elastic energy per unit area stored far ahead of the initial crack)^{6,7}, where E is Young’s modulus. Once G surpasses the minimal quasi-static fracture energy Γ_0 , the tensile (mode-I) crack front starts propagating predominantly in the x direction. Understanding the subsequent spatio-temporal dynamics as a function of $G > \Gamma_0$ remains a major open challenge.

Experiments are limited in probing the real-time spatiotemporal dynamics of cracks in 3D, mainly because continuous imaging of extended dynamic defects that propagate at high velocities inside a material is currently not available. Consequently, large-scale computer simulations offer a powerful complementary approach. The phase-field approach mentioned above allows to numerically solve the 3D problem delineated in Fig. 1a while accurately probing the in silico real-time 3D spatiotemporal dynamics of the crack. This is achieved by solving the linear elastodynamic field equations for $\mathbf{u}(x, y, z, t)$ inside the bar, coupled to an auxiliary field – the scalar phase-field $\phi(x, y, z, t)$ ^{9,12,13,34} (see also “Methods”). The latter satisfies its own dissipative field equation, which features a characteristic dissipation length ξ and a dissipation time τ ^{9,12,13,34} (see also “Methods”).

In the presence of the intense, nearly singular deformation fields in the vicinity of the moving crack front, $\phi(x, y, z, t)$ both spontaneously generates the traction-free surfaces that define the crack^{9,12,13,34} – and hence self-consistently selects the crack trajectory – and gives rise to a rate-dependent fracture energy $\Gamma(v)$ controlled by the dissipation time τ , where v is the crack velocity (note that $\Gamma(v \rightarrow 0) = \Gamma_0$). Both features are absent in sharp-interface approaches based on the classical theory of fracture, Linear Elastic Fracture Mechanics (LEFM)^{6,7}. Another major advantage of this computational approach, essential for the present work, is the ability to tune material properties in a controlled manner in ways that are difficult to achieve in the laboratory. The phase-field fracture approach played a central role in recent progress in understanding rapid crack dynamics in 2D^{9,12,13}. The latter corresponds to taking the $L_z/\xi \rightarrow 0$ limit in the 3D setup of Fig. 1a, leading to a long strip configuration^{6,7}.

In Fig. 2, we plot (green circles) the imposed crack driving force G/Γ_0 against the resulting steady-state crack velocity v (normalized by the shear wave-speed c_s) obtained in 2D phase-field calculations in a homogeneous material¹³. It is observed that G is a monotonically increasing function of v , where each point along the curve corresponds to a straight crack that respects the global tensile (mode-I) symmetry of the system. Moreover, the curve is linear up to a velocity close to the Rayleigh wave-speed, here $c_R = 0.93c_s$, which is predicted to be the upper bound on the velocity of cracks based on LEFM in the absence of symmetry-breaking instabilities^{6,7}. Beyond this regime, G strongly increases with v due to crack tip blunting, leading to increased dissipation^{9,13}.

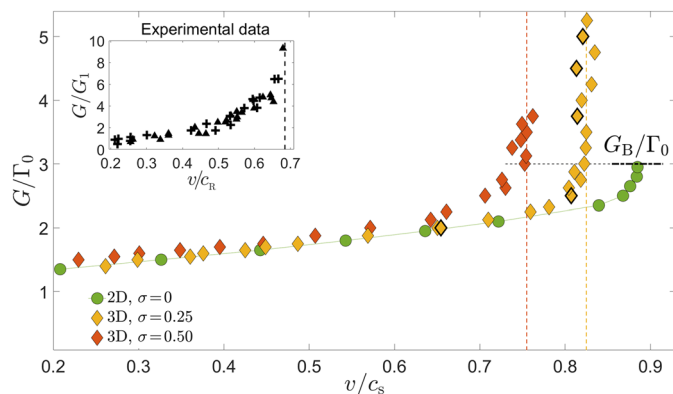


Fig. 2 | The crack driving force as a function of its propagation velocity in 2D and 3D, under different levels of disorder, and the emergence of a limiting crack velocity. (Main) The crack driving force G/Γ_0 vs. steady-state crack velocity v/c_s for a 2D homogeneous material (green circle) and two 3D heterogeneous materials with $\sigma > 0$ (yellow diamonds for $\sigma = 0.25$ and brown diamonds for $\sigma = 0.50$), obtained in phase-field simulations. The thick-boundary diamonds correspond to the 5 snapshots shown in Fig. 3. Steady-state solutions in 2D homogeneous materials do not exist for $G > G_B$ (horizontal dashed-dotted line), upon which a linear branching instability sets in (see Fig. 1b). In 3D materials, the average steady-state crack velocity is bounded by a σ -dependent limiting velocity $v_{\text{lim}}(\sigma)$ (vertical dashed lines), where G increases in a critical-like manner. (Inset) G (normalized by the first data point G_1) vs. steady-state crack velocity v/c_R measured in experiments on a glassy polymer (Polymethyl Methacrylate, PMMA), data extracted from Fig. 3 of ref. 30 (the different symbols correspond to different values of L_z , see ref. 30). The vertical dashed line, highlighting the similarity to the simulation data in the main panel, is added as a guide to the eye. Similar observations for additional materials are provided in Fig. 17 of ref. 2. Source data are provided as a Source Data file.

The 2D G vs. v curve terminates at G_B (horizontal dashed-dotted line), at a velocity very close to – yet slightly smaller than – c_R , upon which a branching instability (sometimes termed macro-branching/tip-splitting) takes place. That is, a straight tensile crack branches/splits into two co-existing cracks^{9,13}, shown in Fig. 1b, providing a mechanism for excess dissipation due to additional fracture surfaces^{40,41}. For $G > G_B$, steady-state solutions no longer exist in 2D. The high-velocity 2D branching instability, previously demonstrated in refs. 9,13, has been experimentally observed in quasi-2D brittle materials^{9,15,23,29,42–44}. Finally, since in steady-state G is balanced by the fracture energy, we identify the G vs. v curve as $\Gamma_{2D}(v)$ for strictly homogeneous 2D materials, and hence the 2D branching velocity v_B corresponds to $\Gamma_{2D}(v_B) = G_B$. We note in passing that the 2D oscillatory instability, which emerges at a velocity slightly smaller than v_B ¹², does not emerge here (see “Methods”).

Branching in 2D exists in purely homogeneous materials and hence is a linear instability. We next considered the effect of dimensionality on the stability of cracks in homogeneous materials by studying 3D systems with a finite thickness L_z , as in Fig. 1a, driven by $G < G_B$. We found that tensile cracks in our 3D homogeneous system are remarkably stable, both linearly and nonlinearly. In particular, for a wide variety of crack shape perturbations (of different spatial extent and amplitudes) as well as for a wide range of isolated heterogeneities (of different sizes, shapes and locations), cracks transiently go out of their initial plane but then decay back to the tensile symmetry plane. That is, no persistent 3D out-of-plane crack instabilities exist in homogeneous materials for $G < G_B$, hence for $v < v_B$ (persistent in-plane crack front waves are triggered, as discussed very recently in ref. 34). This is in sharp and qualitative disagreement with a wide range of experimental observations that show that tensile cracks in 3D brittle amorphous materials reveal persistent out-of-plane structures at velocities smaller than v_B , as already noted above.

What is the origin of this understanding gap? What is the crucial physical ingredient missing? In order to gain insight into these

fundamental questions, we stress that the experimental evidence at hand was obtained for amorphous materials, which are homogeneous at macroscopic scales, but feature disorder at smaller scales. The quantitative characterization and understanding of disordered materials is still incomplete; in particular, while it is known that various material properties (e.g., elastic moduli^{45,46}) feature significant fluctuations over supermolecular lengthscales, we do not yet have robust and quantitative knowledge of the statistics of fundamental physical quantities such as the fracture energy. Consequently, in order to test the possible importance of material quenched disorder, our strategy would be to adopt minimal assumptions about material quenched disorder and explore its implications for bridging the qualitative gap in our understanding of 3D dynamic fracture.

Specifically, we introduce quenched disorder in the form of a Gaussian distribution in the dimensionless quasi-static ($v \rightarrow 0$) fracture energy Γ/Γ_0 , with unity mean, standard deviation determined by σ and spatial correlation length R (see “Methods”). We hereafter set $R = 10\xi$ and study the effect of σ on 3D dynamic fracture. In Fig. 2, we plot (diamonds) G/Γ_0 against the average steady-state crack velocity v/c_s obtained in 3D phase-field calculations as in Fig. 1a, for two values of σ . Recall that in steady state, energy balance implies $\Gamma(v) = G$ ^{6,7}, where $\Gamma(v)$ is the actual fracture energy. It is observed that $\Gamma(v) = G$ closely follows the 2D homogeneous material curve at relatively small v , then it deviates from it at larger v 's until it reaches a limiting (terminal) velocity $v_{\text{lim}}(\sigma) < v_B < c_R$, consistently with numerous experiments (e.g., refs. 2,21 and the compilation of experimental works in Table 1 of ref. 15). Moreover, $d\Gamma/dv$ appears to diverge for $v \rightarrow v_{\text{lim}}$, also consistently with experiments²¹, cf. inset of Fig. 2.

The results in Fig. 2 can be described by the steady-state energy balance

$$\Gamma(v) = \Gamma_{2D}(v) + \delta\Gamma_{3D}(v, \sigma) = G, \quad (1)$$

where $\delta\Gamma_{3D}(v, \sigma)$ corresponds to 3D disorder-induced corrections to the 2D homogeneous material $\Gamma_{2D}(v)$. We note that we do not explicitly incorporate the dependence of $\delta\Gamma_{3D}(v, \sigma)$ on the correlation length R since it is kept constant, as stated above. Moreover, note that $\delta\Gamma_{3D}(v, \sigma)$ accounts for both dimensionality (3D vs. 2D) and for quenched disorder; results on the effect of finite quenched disorder in 2D are presented in the Supplementary Information, and are further discussed below. It is observed in Fig. 2 that for relatively small velocities, we have $\delta\Gamma_{3D}(v, \sigma) \ll \Gamma_{2D}(v) \simeq \Gamma(v)$, and the behavior essentially identifies with that of 2D homogeneous materials. At some σ -dependent characteristic v , $\delta\Gamma_{3D}(v, \sigma)$ is no longer negligible compared to $\Gamma_{2D}(v)$, i.e., 3D disorder-induced effects become important. Finally, as $v \rightarrow v_{\text{lim}}$, $\delta\Gamma_{3D}(v, \sigma)$ becomes sizable/dominant and appears to feature a critical behavior, i.e., $d\Gamma(v)/dv$ appears to diverge. Our main challenge in the remaining of the paper is to understand the physics behind $\delta\Gamma_{3D}(v, \sigma)$.

Out-of-plane crack structures and the localized branching instability

To start addressing this challenge, we focus on out-of-plane crack structures that correspond to the 3D results in Fig. 2 with $\sigma = 0.25$ (to be considered hereafter). Since the crack front experiences both in- and out-of-plane fluctuations, the quantity v hereafter stands for the averaged front velocity (see “Methods”). We take advantage of our computational platform and consider out-of-plane crack structures inside the bulk of the material, not just their fractographic signature (i.e., the patterns left on the postmortem fracture surface). In Fig. 3 (left column), we present a sequence of out-of-plane crack structures as a function of the crack driving force G , covering the various regimes of interest (the data points used are marked by thick boundaries in Fig. 2).

Figure 3a corresponds to $G/\Gamma_0 = 2$, for which $\delta\Gamma_{3D}(v, \sigma) \ll \Gamma_{2D}(v)$. It is observed that out-of-plane protrusions are very rare and small, i.e., the crack is essentially planar (mirror-like), which is consistent with the

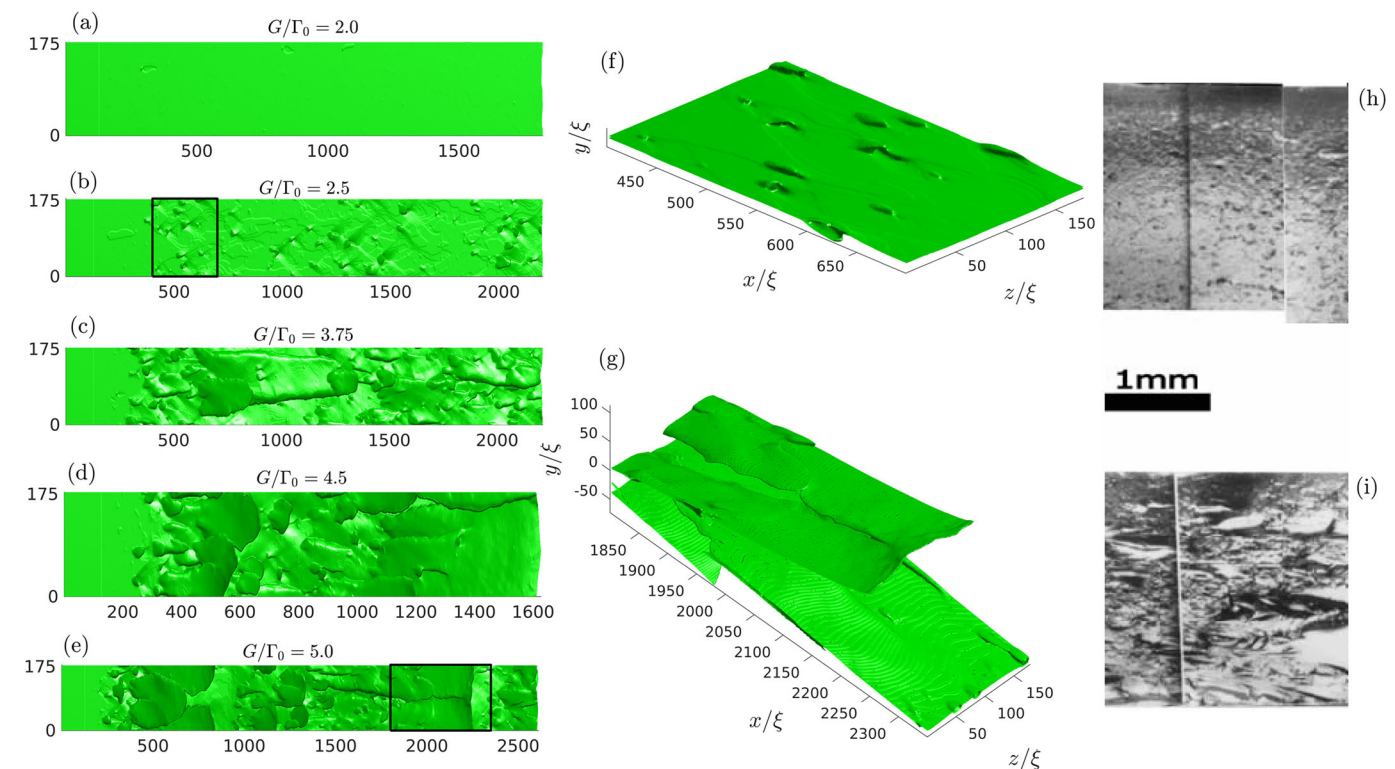


Fig. 3 | Out-of-plane 3D fracture structures in the theoretical model and in experiments, and the mirror-mist-hackle-macro-branching sequence of morphological transitions. **a–e** (left column) Uppermost out-of-plane crack structures – corresponding to the phase-field $\phi(\mathbf{x}) = 1/2$ iso-surface – inside the bulk (top view), for the five G values indicated (corresponding to the thick-boundary diamonds in Fig. 2), see text for extensive discussion. In each panel, the long axis is the propagation (x) direction and the perpendicular one in the crack front direction (z -axis). Both axes are expressed in units of ξ , and the basic length along z is twice that of along x , for visual clarity. The initial crack front is marked by the bright line in the left part of each panel. **f, g** (middle column) Tilted zoom-in 3D view of the regions marked by the rectangles in panels (**b**) and (**e**), respectively. See text for discussion. **h, i** (right column) Fracture surface morphologies (fractography)

measured in 3D dynamic fracture experiments (the crack propagates from left to right) in glass, adapted with permission from Fig. 3b of ref. 28 (image concatenation appears in the original, see ref. 28, and the scale bar is the same for both panels). Panel (**h**) shows the mist region (the preceding mirror region is not shown, but is clearly observed in panel (**a**)), which is characterized by rather isolated, small-amplitude out-of-plane surface structures. Panel (**h**) bears qualitative similarities to panels (**b**) and (**f**). Panel (**i**) shows the hackle region, appearing at larger crack propagation distances in the same experiment, continuously emerging from the mist region that preceded it. The observed wider and elongated out-of-plane surface structures bear clear similarities to panels (**c**) and (**d**). Similar fractographic morphologies are observed in numerous other experiments, e.g., see Fig. 4 in ref. 29, reporting on 3D fracture experiments in a glassy polymer (PMMA).

agreement between $\Gamma(v)$ and $\Gamma_{2D}(v)$ in this regime. Figure 3b corresponds to $G/G_0 = 2.5$, where the deviation of $\Gamma(v)$ from $\Gamma_{2D}(v)$ is still small. It is observed that out-of-plane structures of width Δz and length Δx (see Supplementary Fig. 1), emerge at a significantly higher probability compared to panel (**a**). The out-of-plane structures, leading to a misty fracture surface, are mainly localized branching events of characteristic width comparable to the disorder correlation length $R = 10\xi$, as highlighted in the tilted zoom-in view in Fig. 3f. The out-of-plane profile of asymmetric localized branches (i.e., when the up-down symmetry is broken) is consistent with experiments, see Supplementary Fig. 2. In addition, each localized branching event is accompanied by V-shaped tracks (clearly observed in Fig. 3f), which are reminiscent of typical tracks left by crack front waves^{34,47–49}. Indeed, the propagation velocity of these tracks is consistent with that of crack front waves, see Supplementary Fig. 1.

The character of the out-of-plane structures appearing in Fig. 3c, corresponding to $G/G_0 = 3.75$, qualitatively changes. The localized branching events therein become significantly wider and longer, i.e., leading to hackle-like structures featuring larger Δz and Δx , hence larger areas. With increasing G , as in Fig. 3d, e, Δz and Δx further increase. In Fig. 3e, the width Δz becomes (statistically) comparable to the system thickness L_z , which implies that 2D symmetry is statistically restored. This 3D-to-2D transition is manifested in branching events that are no longer localized, i.e., can be regarded as macro-branches^{15,23,35,36,42} since they capture the entire system thickness and

propagate sizable distances, as highlighted in the tilted zoom-in view in Fig. 3g. Figure 3c–e correspond to G values for which the crack reached the limiting velocity, $v \rightarrow v_{lim}$, where $\delta\Gamma_{3D}(v, \sigma)$ makes a sizable/dominant contribution to $\Gamma(v)$ and $d\Gamma(v)/dv$ appears to diverge.

The probabilistic crossover between Fig. 3a and b closely resembles the widely observed mirror-to-mist transition in brittle amorphous materials^{25–27,29}, see Fig. 3h. The transition in out-of-plane crack structures observed between Fig. 3b, c bears strong similarity to the widely documented mist-to-hackle transition, see Fig. 3i, observed in many brittle amorphous materials, including glassy polymers (e.g., ref. 29) and silica glasses (e.g., refs. 27,28). Moreover, the 3D-to-2D transition, which is accompanied by macroscopic crack branching and follows the hackle regime with increasing crack driving force G , is also well documented in the very same materials (e.g., refs. 15,23,27,29). The correspondence between our findings and a wide range of experimental observations will be further discussed once we gain a deeper understanding of the former.

A physical picture and supporting numerics

Our first goal is to understand the emergence of the localized branching instability in 3D, along with its statistical and dynamical properties. The 2D branching instability in homogeneous materials (Figs. 1b, 2) is triggered at a critical driving force G_B/G_0 (see horizontal dashed-dotted line in Fig. 2). What is the relevance of this instability in 3D in the presence of disorder?

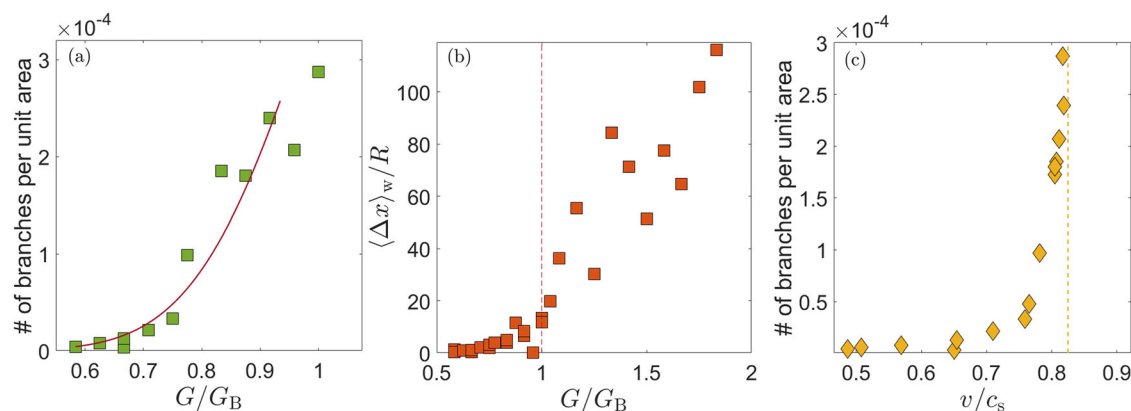


Fig. 4 | The properties of localized branching events at various crack driving forces. **a** The number of branches per unit planar area as a function of $G/G_B \leq 1$ (squares). The solid line corresponds to the prediction in Eq. (2), where $\sigma_R = 0.233$ is independently predicted (see Supplementary Information), and the overall

amplitude is set to agree with the first data point. **b** The normalized weighted branch length $\langle \Delta x \rangle_w / R$ (see text for definition) vs. G/G_B . The vertical dashed line marks $G = G_B$. **c** The same as panel (a), but vs. v . The vertical dashed line corresponds to v_{lim} , as in Fig. 2. Source data are provided as a Source Data file.

On the scale of the correlation scale R , the disordered material can be viewed as locally 2D. Assuming that G in this regime of the 3D dynamics is rather homogeneously distributed along the thickness (z -axis), we expect every fluctuation $\bar{\Gamma}$ in the quasi-static fracture energy that satisfies $\bar{\Gamma}/\Gamma_0 > G/G_B$ to give rise to a localized branching event on a scale R . Rearranging the inequality to read $\bar{\Gamma}/\Gamma_0 < G/G_B$ and assuming localized branching events to be independent of one another in this regime such that the Gaussian (normal) distribution of $\bar{\Gamma}/\Gamma_0$ (with unit mean and standard deviation σ) can be invoked, we obtain (see Supplementary Information)

$$p(G; \sigma) \sim 1 + \operatorname{erf}\left(\frac{G/G_B - 1}{\sigma_R}\right). \quad (2)$$

Here $p(G; \sigma)$ is the localized branching probability, $\operatorname{erf}(\cdot)$ is the error function, which varies super-exponentially with its argument, and $\sigma_R - \sigma$ is the renormalized strength of disorder on a scale R .

Equation (2) predicts an extremely small localized branching probability at small G values and a strong increase of the probability with increasing G below G_B , in qualitative agreement with the results Fig. 3a, b. To more directly test the prediction in Eq. (2), we plot in Fig. 4a the number of localized branches per unit planar area, which is proportional to $p(G; \sigma)$, as a function of $G < G_B$. It is observed that the simple model agrees with the data reasonably well when G is not too close to G_B .

While 2D branching is a linear instability triggered in purely homogeneous materials (that can be realized in silico) by infinitesimal noise, the corresponding 3D localized branching events with $\bar{\Gamma}/\Gamma_0 < G/G_B$ are finite-disorder instabilities and hence are non-perturbative with respect to a homogenized material. Moreover, 3D localized branching events with $\bar{\Gamma}/\Gamma_0 < G/G_B < 1$ are expected to be rather compact, roughly of linear scale R , and hence short-lived and contributing small excess fracture surface. The reason for this is that while localized branching can be triggered with $G/G_B < 1$, it cannot be sustained over scales significantly larger than R (since large local fracture energy fluctuations are likely to be encountered). On the other hand, we expect a change in the dynamics of 3D localized branching events for $G > G_B$ since, under these conditions, the branching solution has a sizable probability to be sustained over larger distances – i.e., to feature significantly larger length Δx – while co-existing with the planar crack solution.

To test this expectation, we plot in Fig. 4b $\langle \Delta x \rangle_w / R$, the average of Δx weighted by the branch area (normalized by R), against G/G_B . It is observed that $\langle \Delta x \rangle_w$ indeed significantly grows with G above $G/G_B \simeq 1$ (marked by the vertical dashed line), reaching values much larger than

R , as expected and in qualitative agreement with Fig. 3c–e. We note that we consider the averaged branch length weighted by its area because while at smaller G values branching events are independent of one another (cf. Fig. 3b), for $G > G_B$ branches effectively “screen” the nucleation of other branches and in fact the number of primary branches decreases with increasing G (though secondary structures emerge as well). Moreover, for $G > G_B$, the branch width Δz is no longer expected to inherit its scale from R . Indeed, the results presented in the inset of Fig. 5 indicate a quasi-linear relation between the averaged branch width $\langle \Delta z \rangle$ and length $\langle \Delta x \rangle$. Fluctuations, to be discussed below, also grow significantly with G , eventually corresponding to the statistical 3D-to-2D transition observed in Fig. 3g. Overall, the results indicate that for $G > G_B$, branching length scales become dynamic and a significant extra fracture surface emerges.

The emergence of a limiting velocity and dynamic renormalization of the fracture energy

We are now in a position to rationalize the steady-state dynamics of 3D cracks as encapsulated in Eq. (1) and, in particular, the physics underlying $\delta\Gamma_{3D}(\nu, \sigma)$. The physical picture discussed above and its numerical support indicate that 3D out-of-plane fracture dynamics are related to a branching instability controlled by the driving force G and to quenched disorder, where both the branching probability $p(G; \sigma)$ and the excess fracture surface associated with branching play a role. In particular, at small G the evolution of $p(G; \sigma)$ is dominant, while for $G > G_B$ the extra surface of the branches dominates, with a transition in between. The essential role of the extra fracture surface generated by localized branching in limiting the velocity of cracks has been previously highlighted in refs. 2,21–23.

To relate the above picture to the emergence of a limiting velocity v_{lim} and to the properties of $\delta\Gamma_{3D}(\nu, \sigma)$, we replot in Fig. 4c the number of localized branches per unit planar area of Fig. 4a as a function of ν , i.e., a quantity proportional to $p(\nu; \sigma)$ instead of $p(G; \sigma)$. It is observed that $p(\nu; \sigma)$ appears to feature a diverging derivative as v_{lim} is approached (vertical dashed line). That is, the branching probability $p(\nu; \sigma)$ alone reveals a clear signature of the emergence of a limiting velocity as G approaches G_B . For $G > G_B$, the branching probability does not further grow (as noted above, it actually decreases), but rather the area of the branches increases such that any increase in G is expected to be balanced by excess fracture surface, without increasing ν , leading to an increase in $\delta\Gamma_{3D}(\nu, \sigma)$ at a fixed $\nu = v_{lim}$.

To test this expectation, we define the apparent areal ratio as the total area of the uppermost out-of-plane crack structures inside the bulk (as seen in the top view in the left column of Fig. 3) divided by the nominal (planar) area. The true areal ratio is likely to be larger as

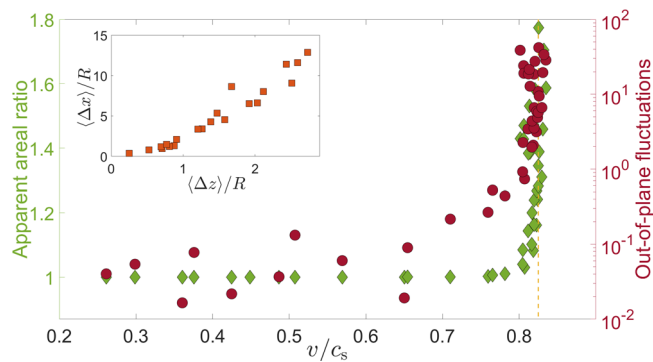


Fig. 5 | Quantification of out-of-plane 3D fracture structures. (Main) The apparent areal ratio (see text for definition) vs. v/c_s (green diamonds, left y-axis). Out-of-plane fluctuations (see text for definition) in units of ξ vs. v/c_s (brown circles, right y-axis, and note the logarithmic scale). The vertical dashed line marks v_{lim} . (Inset) The average branch length $\langle \Delta x \rangle / R$ vs. width $\langle \Delta z \rangle / R$. Source data are provided as a Source Data file.

secondary structures can develop beneath the uppermost out-of-plane crack structures. The apparent areal ratio is plotted (diamonds, left y-axis) in Fig. 5 vs. v and is observed to be indistinguishable from unity until v_{lim} is approached. At $v = v_{\text{lim}}$, the apparent areal ratio increases in a critical-like manner, as expected. It thus supports the idea that the 3D disorder-induced excess dissipation $\delta\Gamma_{3D}(v, \sigma)$ balances any increase in G at $v = v_{\text{lim}}$ by creating extra fracture surface. That is, the fracture energy $\Gamma(v)$ is dynamically renormalized by the out-of-plane spatio-temporal dynamics of the 3D crack.

In the Supplementary Information, we studied the effect of finite quenched disorder on 2D cracks. While we found qualitative differences between 2D and 3D at small G/Γ_0 values (most notably crack arrest in the former, see the Supplementary Information), for large G/Γ_0 values, repeated branching/tip-splitting events in 2D also dynamically renormalize the 2D fracture energy and give rise to a limiting velocity (albeit somewhat less well defined compared to 3D, see the Supplementary Information). Consequently, the emergence of a limiting velocity and the dynamic renormalization of the fracture energy due to the disorder-induced generation of extra fracture surface through branching are qualitatively similar in 2D and 3D, although the associated crack patterns are significantly different.

Finally, we expect fluctuations in 3D out-of-plane crack structures to significantly increase as $v \rightarrow v_{\text{lim}}$. To test this expectation, we extracted for each $(x, y = 0, z)$ point along the original symmetry plane the y difference (in units of ξ) between the uppermost out-of-plane crack location (shown on the left column of Fig. 3) and its lowermost counterpart. We then averaged over all $(x, y = 0, z)$ points and plotted the results in Fig. 5 (circles, right y-axis) vs. v on a log-linear scale. It is observed that the out-of-plane fluctuations are very small for small v (note the logarithmic right y-axis), consistently with the branching probability $p(v; \sigma)$ being small in this regime. Around $v/c_s = 0.7$, the fluctuations start to grow, yet they still make a negligible contribution to the extra fracture area (see diamonds and left y-axis). As $v \rightarrow v_{\text{lim}}$, out-of-plane fluctuations grow significantly, featuring the same critical-like behavior as the apparent areal ratio, as expected from the emerging physical picture.

Discussion

Our results indicate that 3D dynamic fracture in brittle amorphous materials is controlled by two physical ingredients. The first is a 2D linear instability that is characterized by a crack driving force threshold G_B , providing a mechanism for generating extra fracture surface, i.e., for increasing the effective fracture energy. The 2D homogeneous material instability involves a topological change, going beyond a

single crack, in the form of crack branching. The second ingredient is finite-strength quenched disorder that features a spatial correlation length R .

In the presence of finite disorder, the 2D branching instability is transiently excited in 3D at crack driving forces G well below G_B . It features localization over a scale R that breaks translational invariance along the crack front. Upon increasing G in 3D, the localized branching instability becomes longer-lived and features larger lengthscales for $G \simeq G_B$. The extra fracture surface associated with these increasingly larger branches dynamically renormalizes the effective fracture energy, giving rise to a disorder-dependent limiting velocity v_{lim} that the crack cannot surpass. The emergence of v_{lim} is accompanied by a critical-like behavior in which the fracture energy features a divergent variation with the crack velocity. In this regime, for sufficiently large G , branches become so wide that the system statistically recovers translational invariance along the crack front, and branching becomes macroscopic. We also showed, see the Supplementary Information, that a similar mechanism is operative in 2D disordered materials, giving rise to dynamic renormalization of the effective fracture energy and to a disorder-dependent limiting velocity.

This physical picture and its manifestations are consistent with a broad range of 3D experimental observations that were not fully understood previously. At the macroscopic scale, it is widely observed (e.g., in refs. 2,15,21) that cracks in brittle materials attain limiting velocities well below c_R , the ideal theoretical limit^{6,7}. The emergence of a limiting velocity has been previously associated with the generation of extra fracture dissipation accompanying out-of-plane surface structures^{2,21–23}. Our work contributes to understanding the physical origin of these observations, most notably highlighting the basic roles played by finite quenched disorder and its coupling to a 2D instability, as well as the probabilistic, disorder-induced nature of the underlying sequence of transitions. We also highlighted the critical-like behavior of the fracture energy upon approaching v_{lim} , which is consistent with experiments on steady-state cracks, reproduced in the inset of Fig. 2 (similar observations for additional materials are provided in Fig. 17 of ref. 2). At smaller scales, localized instabilities in 3D, mainly in the form of micro-cracking damage^{14–17} and micro-branching^{21–24} that involve a topological change and the generation of extra fracture surface, are widely observed.

The localized branching instability extensively discussed above bears close similarity to the micro-branching instability^{21–24}. The latter features characteristic lengthscales at initiation, most notably minimal micro-branch width and length^{21–24}, consistent with our findings in which the latter are related to the disorder correlation length R . Our results show that localized branching is a probabilistic phenomenon, yet it appears to be rather sharp due to the super-exponential increase of the branching probability at small G , which depends on the finite-strength disorder. The probabilistic nature of the micro-branching instability and its dependence on finite disorder are indeed experimentally demonstrated^{24,50}, in agreement with our findings.

With increasing driving force, micro-branches have been shown to significantly increase in size, to lead to increased effective fracture energy associated with extra fracture surface^{21–23}, to be accompanied by increased out-of-plane fluctuations^{21–23}, to feature a 3D-to-2D transition²¹ and eventually to transform into macro-branches²³, all in agreement with our results. The approximate linear scaling $\langle \Delta x \rangle \sim \langle \Delta z \rangle$, cf. inset of Fig. 5, is also in agreement with experimental micro-branching observations⁴⁷. Finally, the out-of-plane profiles of asymmetric localized branches agree with those of experimentally observed micro-branches, as demonstrated in Supplementary Fig. 2.

At intermediate scales, commonly probed by fractography in experiments, our findings are consistent with, and offer a unifying understanding of, the widely observed sequence of mirror-mist-hackle-macro-branching morphological transitions^{25–29}. This sequence of transitions is commonly observed as a function of crack

propagation distance in experiments that involve accelerating cracks. We take advantage of our computational framework, which allows to simulate very long systems (see “Methods”), to study this sequence of transitions in a controlled manner at the steady-state level as a function of G . Our observations not only (cf. Fig. 3) reproduce this sequence of transitions as G is varied, but we also provide a theoretical understanding of the physics underlying each transition.

The mirror-mist transition is a probabilistic crossover, which is rather sharp due to the super-exponential variation of the localized branching probability for $G < G_B$. Transiently excited localized branching events in this regime are spatially uncorrelated and small, featuring a scale comparable to the disorder correlation length R , responsible for the misty appearance of the fracture surface. The mist-hackle transition occurs at $G \approx G_B$, upon which localized branching events become longer-lived and feature dynamic lengthscales that increase with increasing G . The wider and longer branching events are responsible for the hackle-like appearance of the fracture surface. Finally, at sufficiently large G , branches can capture the entire system thickness L_z , statistically recovering translational symmetry in the thickness direction. This 3D-to-2D transition results in macro-branching.

Our findings also raise some pressing questions for future investigation. A central element in the emerging physical picture is finite-amplitude quenched disorder. In the absence of well-established data about spatial disorder in the fracture energy of amorphous materials, we invoked in our calculations a minimal assumption in the form of a Gaussian disorder characterized by a dimensionless strength σ and correlation length R . It would be most desirable to quantitatively characterize the statistical properties of various important physical quantities in amorphous materials, including the amplitude of fluctuations and their spatial correlation length. A possible indirect way to address this point might be to study surface roughness at low propagation velocities^{3,37}.

Furthermore, we have shown that various quantities, e.g., the onset of localized branching velocity and the limiting velocity v_{lim} , are disorder-dependent. Specifically, v_{lim} is expected to decrease with both increasing disorder strength σ (see Fig. 2) and correlation length R (see the recent, related work in ref. 51). Consequently, extracting the properties of the disorder may lead to a quantitative comparison with experiments. Finally, while our large-scale calculations have been carried out using cutting-edge GPU-based computational platforms (see “Methods”), we cannot yet rule out some finite-size effects in our results, especially with respect to L_y , but possibly also to L_z . Future research, potentially employing enhanced computational power, should shed light on this issue as well.

Methods

The 3D phase-field fracture framework

The 3D phase-field fracture framework we employed has been very recently presented in great detail in the Supplementary Materials file of ref. 34. Here, for completeness, we briefly repeat the main elements of the formulation and highlight specific features of its application in this work. A general material is described in this framework by the following potential energy U , kinetic energy T and dissipation function D ^{9,12,13}

$$U = \int \left[\frac{1}{2} \kappa (\nabla \phi)^2 + g(\phi) e(\mathbf{u}) + w(\phi) e_c \right] dV, \quad (3)$$

$$T = \int \frac{1}{2} f(\phi) \rho (\partial_t \mathbf{u})^2 dV, \quad (4)$$

$$D = \frac{1}{2\chi} \int (\partial_t \phi)^2 dV, \quad (5)$$

in terms of a 3D time-dependent vectorial displacement field $\mathbf{u}(x, y, z, t)$ and a 3D time-dependent auxiliary scalar phase-field $0 \leq \phi(x, y, z, t) \leq 1$. Here, dV is a volume differential and the integration extends over the entire system. The evolution of $\phi(\mathbf{x}, t)$ and $\mathbf{u}(\mathbf{x}, t)$ follows Lagrange's equations

$$\frac{\partial}{\partial t} \left[\frac{\delta L}{\delta (\partial \psi / \partial t)} \right] - \frac{\delta L}{\delta \psi} + \frac{\delta D}{\delta (\partial \psi / \partial t)} = 0, \quad (6)$$

where $L = T - U$ is the Lagrangian and $\psi = (\phi, u_x, u_y, u_z)$, i.e., $\mathbf{u} = (u_x, u_y, u_z)$ are the components of the displacement vector field.

An intact/unbroken material state corresponds to $\phi = 1$, for which $g(\phi) = f(\phi) = 1 - w(\phi) = 1$. It describes a non-dissipative, elastodynamic material response characterized by an energy density $e(\mathbf{u})$. For the latter, we use the linear elastic energy density

$$e(\mathbf{u}) = \frac{1}{2} \lambda \text{tr}^2(\boldsymbol{\varepsilon}) + \mu \text{tr}(\boldsymbol{\varepsilon}^2), \quad (7)$$

where $\boldsymbol{\varepsilon} = \frac{1}{2} [\nabla \mathbf{u} + (\nabla \mathbf{u})^T]$ is the infinitesimal (linearized) strain tensor, and λ and μ (shear modulus) are the Lamé coefficients. We set $\lambda = 2\mu$ in all of our calculations.

Dissipation, loss of load-bearing capacity and eventually fracture accompanied by the generation of traction-free surfaces are associated with a strain energy density threshold e_c . When the latter is surpassed, ϕ decreases from unity, and the degradation functions $g(\phi)$, $f(\phi)$ and $1 - w(\phi)$ also decrease from unity towards zero, upon which complete fracture takes place. We adopt the so-called KKL choice of the degradation functions^{13,31}, corresponding to $f(\phi) = g(\phi)$ and $w(\phi) = 1 - g(\phi)$, with $g(\phi) = 4\phi^3 - 3\phi^4$. This choice, together with the linear elastic strain energy density in Eq. (7) (that implies a vanishing nonlinear elastic zone near the crack front^{9,12,13}), suppresses the 2D oscillatory instability¹³. The reason for this choice is that the 2D oscillatory instability, unlike the 2D tip-splitting instability, does not involve a topological change and hence does not manifest itself in 3D in a thickness-localized manner (again, unlike the 2D tip-splitting instability). Therefore, we use the KKL choice of the degradation functions, which is more computationally robust in the presence of continuous disorder compared to its alternative discussed in ref. 13.

The resulting set of nonlinear partial differential field equations features a dissipation lengthscale $\xi = \sqrt{\kappa/2e_c}$ near crack fronts and an associated dissipation timescale $\tau = (2\chi e_c)^{-1}$. Upon expressing length in units of ξ , time in units of ξ/c_s , energy density in units of μ and the mass density ρ in units of μ/c_s^2 ($c_s = \sqrt{\mu/\rho}$ is the shear wave-speed), the dimensionless set of equations depends on just two dimensionless parameters: e_c/μ and $\beta = \tau c_s/\xi$. The latter controls the ν -dependence of the fracture energy, $\Gamma(\nu)$ ^{9,12,13}. In our calculations, we set $e_c/\mu = 0.01$ and $\beta = 2.76$. We also set $L_y = 256\xi$ and $L_z = 179\xi$, where L_x is essentially indefinitely large due to an employed treadmill procedure¹³. The boundary conditions are specified above, and the details of the numerical implementation are provided in ref. 34. Each calculation is performed on a single GPU (NVIDIA RTX A6000 or NVIDIA A40), either owned by the Bouchbinder group or available on one of the computer clusters at the Weizmann Institute of Science. A typical 3D simulation time (e.g., one of those shown in the leftmost column of Fig. 3) is ~5 days.

Continuous quenched disorder

In ref. 34, we considered only isolated/discrete material heterogeneities (asperities). In the present work, we incorporated continuous quenched disorder into the phase-field framework, which was shown above to play essential roles in 3D dynamic fracture. Continuous quenched disorder is introduced in two steps. First, as in ref. 34, we define a dimensionless auxiliary quenched disorder field $\zeta(\mathbf{x})$, which can be coupled to any physical parameter in the problem. This

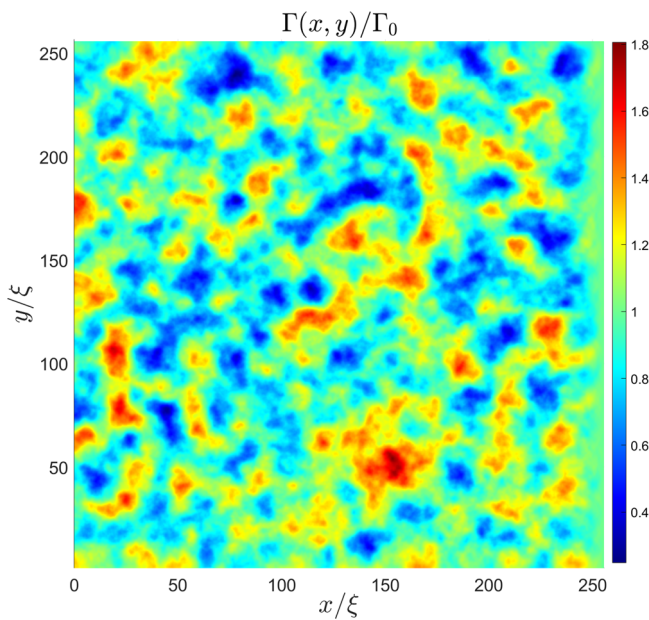


Fig. 6 | An example of a planar cut of a 3D static fracture energy disorder field. A 2D x - y cut of a single realization of the $\Gamma(\mathbf{x})$ disorder field generated with $\sigma = 0.25$ and $R = 10\xi$. The spatial correlation length R of the quenched disorder is evident.

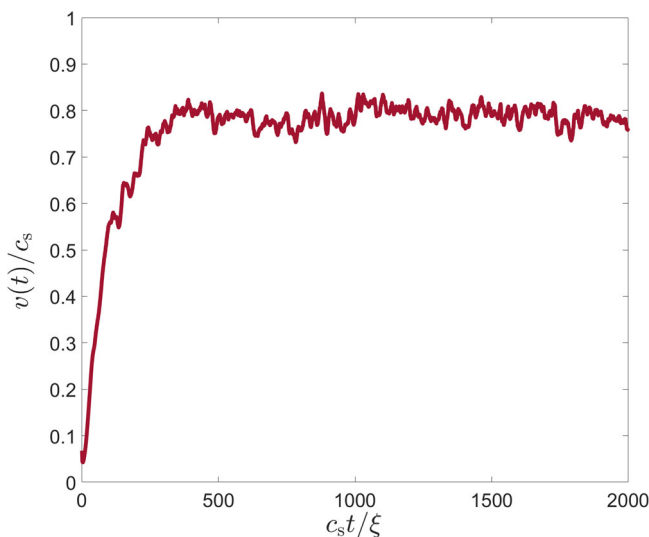


Fig. 7 | An example of the time evolution of the average crack front velocity. The average crack front velocity $v(t)/c_s$, as defined in the text, plotted against $c_s t/\xi$ for $G/\Gamma_0 = 2.25$ (with our generic quenched disorder parameters $\sigma = 0.25$ and $R = 10\xi$). It is observed that after an initial acceleration phase, the crack settles into a statistical steady state (defining the mean velocity v per G , accompanied by temporal fluctuations), where our analysis is performed. Source data are provided as a Source Data file.

coupling is achieved by transforming an originally spatially uniform parameter α_0 into a field of the form $\alpha(\mathbf{x}) = \alpha_0[1 + \alpha_\zeta \zeta(\mathbf{x})]$, where $0 \leq \alpha_\zeta \leq 1$ is a dimensionless coupling coefficient.

Above, $-1 \leq \zeta(\mathbf{x})$ is taken to follow a Gaussian distribution of width σ and zero mean, i.e., ζ at each spatial point \mathbf{x} (in practice, at each numerical grid point) is extracted from a normal distribution with standard deviation σ and zero mean, with no spatial correlations. That is, ζ at a given spatial location is independent of its value at other locations. The value of σ is used to quantify the strength of disorder

throughout the manuscript. Note that the choice $-1 \leq \zeta(\mathbf{x})$ ensures that $\alpha(\mathbf{x}) \geq 0$ for any $0 \leq \alpha_\zeta \leq 1$, and hence the procedure can be naturally applied to positive physical quantities (e.g., the fracture energy and/or the shear modulus). The Gaussian probability associated with $-\infty < \zeta(\mathbf{x}) < -1$ is small in our calculations, and the way it is taken into account is further discussed below.

In the second step, spatial correlations in the quenched disorder are introduced. To this aim, we define a spatial kernel $K(\mathbf{x})$ of compact support R , of the form $K(\mathbf{x}) = 1 - (|\mathbf{x}|/R)^5$ for $|\mathbf{x}| \leq R$ and zero otherwise. Then the actual value of the physical parameter of interest at a point \mathbf{x} , say $\tilde{\alpha}(\mathbf{x})$, is obtained through a convolution of $\alpha(\mathbf{x})$ with the kernel $K(\mathbf{x})$, i.e., $\tilde{\alpha}(\mathbf{x}) = K(\mathbf{x}) * \alpha(\mathbf{x})$. Consequently, $\tilde{\alpha}(\mathbf{x})$ features a spatial correlation length R . In this work, we set $\alpha_\zeta = 0.9$ (that renormalizes the disorder strength) and $R = 10\xi$. The above procedure for introducing quenched disorder in any physical parameter is applied in this work for the quasi-static ($\nu \rightarrow 0$) fracture energy Γ_0 .

It is known that $\Gamma_0 \sim e_c \xi \sim \sqrt{\kappa e_c}^{9,12,13}$ and recall that $\beta = \tau c_s / \xi \sim (\chi e_c \xi)^{-1}$ (i.e., with $\tau \sim (\chi e_c)^{-1}$). Consequently, we can simultaneously couple κ , e_c and χ^{-1} to the very same realization of the quenched disorder field $\zeta(\mathbf{x})$ (with the same α_ζ) such that the quasi-static fracture energy features quenched disorder, while $\xi \sim \sqrt{\kappa/e_c}$ and $\beta \sim (\chi e_c \xi)^{-1}$ are kept fixed (i.e., independent of \mathbf{x}). This way, the dimensionless quasi-static fracture energy – denoted by $\bar{\Gamma}/\Gamma_0$ – follows a Gaussian distribution with unity mean, standard deviation $\alpha_\zeta \sigma$ and spatial correlation length R , as stated above, while its rate dependence (variation with ν , which is controlled by β) is spatially uniform. A 2D cut of a single realization of the $\Gamma(\mathbf{x})$ disorder field is presented in Fig. 6.

The average crack velocity

A central quantity in this work is the average crack front velocity v . In the presence of quenched disorder, the crack front does not generally remain a continuous line propagating in a 3D space. As extensively shown above, not only can it be seriously distorted and meander out of the symmetry plane, but it actually undergoes various topological changes as the crack develops localized branches, hierarchical facets, segmentation and more. In view of these complex structures, the average crack front velocity v is operationally defined as follows: at each point in time t , the crack is defined through the phase-field $\phi(\mathbf{x}, t) = 1/2$ iso-surface. Then, we find the intersection of this iso-surface with the x - y plane associated with every z value. The intersection point with the largest x coordinate (the crack propagates in the positive x direction) corresponds to the front position $\mathbf{f}(z, t) = (f_x(z, t), f_y(z, t))$. Finally, the average crack front velocity $v(t)$ is obtained as the z -average of $\partial f_x(z, t)$, i.e., $v(t) = \langle \partial f_x(z, t) \rangle_z$. When the crack reaches a statistical steady state, $v(t)$ features a plateau that defines the steady-state velocity v (for each G), accompanied by temporal fluctuations, as demonstrated in Fig. 7.

The quantification of out-of-plane fracture structures

The uppermost out-of-plane crack structures shown in Fig. 3 are obtained as follows: the $\phi(\mathbf{x}) = 1/2$ iso-surface at the end of each phase-field simulation is considered. Then, at each (x, z) point, we construct a vertical line along y and find the uppermost y intersection with the $\phi(\mathbf{x}) = 1/2$ iso-surface. The resulting surface is plotted in Fig. 3 for different G values. The apparent areal ratio, plotted in Fig. 5 (left y -axis), is obtained as the total area of the uppermost out-of-plane surface divided by the corresponding nominal (planar) area, as noted above. The true areal ratio is, in fact, larger as secondary structures develop beneath the uppermost out-of-plane crack surface at large G , as noted above.

Finally, calculating the out-of-plane fluctuations – that are plotted in Fig. 5 (right y -axis) – involves also the lowermost out-of-plane surface, which is obtained similarly to the uppermost one, just for the lowermost y intersection of vertical lines with the $\phi(\mathbf{x}) = 1/2$ iso-surface (note that the uppermost and lowermost surfaces are not symmetric,

i.e., the up-down symmetry is broken, see also Supplementary Information). The average over (x, z) of the difference between the uppermost and lowermost surfaces (in units of ξ) provides a measure of out-of-plane fluctuations.

Data availability

The datasets generated and analyzed in this study, corresponding to a few terabytes of data, will be made available upon request and the availability of a suitable storage space. Source data are provided with this paper.

Code availability

The simulation and data analysis codes used to generate the results reported in this work will be made available upon request.

References

- Ravi-Chandar, K. Dynamic fracture of nominally brittle materials. *Int. J. Fract.* **90**, 83 (1998).
- Fineberg, J. & Marder, M. Instability in dynamic fracture. *Phys. Rep.* **313**, 1 (1999).
- Bonamy, D. & Bouchaud, E. Failure of heterogeneous materials: a dynamic phase transition? *Phys. Rep.* **498**, 1 (2011).
- Bouchbinder, E., Goldman, T. & Fineberg, J. The dynamics of rapid fracture: instabilities, nonlinearities and length scales. *Rep. Prog. Phys.* **77**, 046501 (2014).
- Fineberg, J. & Bouchbinder, E. Recent developments in dynamic fracture: some perspectives. *Int. J. Fract.* **196**, 33 (2015).
- Freund, L. B. *Dynamic Fracture Mechanics* (Cambridge Univ. Press, 1990).
- Broberg, K. R. *Cracks and Fracture* (Academic Press, 1999).
- Livne, A., Ben-David, O. & Fineberg, J. Oscillations in rapid fracture. *Phys. Rev. Lett.* **98**, 124301 (2007).
- Lubomirsky, Y., Chen, C.-H., Karma, A. & Bouchbinder, E. Universality and stability phase diagram of two-dimensional brittle fracture. *Phys. Rev. Lett.* **121**, 134301 (2018).
- Bouchbinder, E., Livne, A. & Fineberg, J. Weakly nonlinear theory of dynamic fracture. *Phys. Rev. Lett.* **101**, 264302 (2008).
- Bouchbinder, E. Dynamic crack tip equation of motion: high-speed oscillatory instability. *Phys. Rev. Lett.* **103**, 164301 (2009).
- Chen, C.-H., Bouchbinder, E. & Karma, A. Instability in dynamic fracture and the failure of the classical theory of cracks. *Nat. Phys.* **13**, 1186 (2017).
- Vasudevan, A., Lubomirsky, Y., Chen, C.-H., Bouchbinder, E. & Karma, A. Oscillatory and tip-splitting instabilities in 2D dynamic fracture: the roles of intrinsic material length and time scales. *J. Mech. Phys. Solids* **151**, 104372 (2021).
- Ravi-Chandar, K. & Knauss, W. An experimental investigation into dynamic fracture: II. Microstructural aspects. *Int. J. Fract.* **26**, 65 (1984).
- Ravi-Chandar, K. & Knauss, W. G. An experimental investigation into dynamic fracture: III. On steady-state crack propagation and crack branching. *Int. J. Fract.* **26**, 141 (1984).
- Scheibert, J., Guerra, C., Célerié, F., Dalmas, D. & Bonamy, D. Brittle-quasibrittle transition in dynamic fracture: an energetic signature. *Phys. Rev. Lett.* **104**, 045501 (2010).
- Guerra, C., Scheibert, J., Bonamy, D. & Dalmas, D. Understanding fast macroscale fracture from microcrack post mortem patterns. *Proc. Natl Acad. Sci. USA* **109**, 390 (2012).
- Tanaka, Y., Fukao, K., Miyamoto, Y. & Sekimoto, K. Discontinuous crack fronts of three-dimensional fractures. *Europhys. Lett.* **43**, 664 (1998).
- Kolvin, I., Cohen, G. & Fineberg, J. Topological defects govern crack front motion and facet formation on broken surfaces. *Nat. Mater.* **17**, 140 (2018).
- Baumberger, T., Caroli, C., Martina, D. & Ronsin, O. Magic angles and cross-hatching instability in hydrogel fracture. *Phys. Rev. Lett.* **100**, 178303 (2008).
- Sharon, E. & Fineberg, J. Microbranching instability and the dynamic fracture of brittle materials. *Phys. Rev. B* **54**, 7128 (1996).
- Sharon, E. & Fineberg, J. Universal features of the microbranching instability in dynamic fracture. *Philos. Mag. B* **78**, 243 (1998).
- Sharon, E. & Fineberg, J. The dynamics of fast fracture. *Adv. Eng. Mater.* **1**, 119 (1999).
- Livne, A., Cohen, G. & Fineberg, J. Universality and hysteretic dynamics in rapid fracture. *Phys. Rev. Lett.* **94**, 224301 (2005).
- Lawn, B. *Fracture of Brittle Solids* (Cambridge Univ. Press, 1993).
- Johnson, J. & Holloway, D. Microstructure of the mist zone on glass fracture surfaces. *Philos. Mag.* **17**, 899 (1968).
- Rabinovitch, A., Belizovsky, G. & Bahat, D. Origin of mist and hackle patterns in brittle fracture. *Phys. Rev. B* **61**, 14968 (2000).
- Rabinovitch, A. & Bahat, D. Mirror-mist transition in brittle fracture. *Phys. Rev. E* **78**, 067102 (2008).
- Jiao, D., Qu, R. T. & Zhang, Z. F. Macroscopic bifurcation and fracture mechanism of polymethyl methacrylate. *Adv. Eng. Mater.* **17**, 1454 (2015).
- Sharon, E., Gross, S. P. & Fineberg, J. Energy dissipation in dynamic fracture. *Phys. Rev. Lett.* **76**, 2117 (1996).
- Karma, A., Kessler, D. & Levine, H. Phase-field model of mode III dynamic fracture. *Phys. Rev. Lett.* **87**, 45501 (2001).
- Karma, A. & Lobkovsky, A. E. Unsteady crack motion and branching in a phase-field model of brittle fracture. *Phys. Rev. Lett.* **92**, 245510 (2004).
- Hakim, V. & Karma, A. Laws of crack motion and phase-field models of fracture. *J. Mech. Phys. Solids* **57**, 342 (2009).
- Das, S., Lubomirsky, Y. & Bouchbinder, E. Dynamics of crack front waves in three-dimensional material failure. *Phys. Rev. E* **108**, L043002 (2023).
- Bleyer, J. & Molinari, J.-F. Microbranching instability in phase-field modelling of dynamic brittle fracture. *Appl. Phys. Lett.* **110**, 151903 (2017).
- Henry, H. & Adda-Bedia, M. Fractographic aspects of crack branching instability using a phase-field model. *Phys. Rev. E* **88**, 060401 (2013).
- Ponson, L. Fracture mechanics of heterogeneous materials: effective toughness and fluctuations in *Mechanics and Physics of Fracture: Multiscale Modeling of the Failure Behavior of Solids*, 207–254 (Springer, 2023).
- Roch, T., Lebihain, M. & Molinari, J.-F. Dynamic crack-front deformations in cohesive materials. *Phys. Rev. Lett.* **131**, 096101 (2023).
- Lebihain, M., Leblond, J.-B. & Ponson, L. Effective toughness of periodic heterogeneous materials: the effect of out-of-plane excursions of cracks. *J. Mech. Phys. Solids* **137**, 103876 (2020).
- Eshelby, J. Energy relations and the energy-momentum tensor in continuum mechanics in *Inelastic Behaviour of Solids*, 77–115 (McGraw-Hill, 1970).
- Katzav, E., Adda-Bedia, M. & Arias, R. Theory of dynamic crack branching in brittle materials. *Int. J. Fract.* **143**, 245 (2007).
- Kobayashi, A., Wade, B., Bradley, W. & Chiu, S. Crack branching in homalite-100 sheets. *Eng. Fract. Mech.* **6**, 81 (1974).
- Sun, Y., Edwards, M. G., Chen, B. & Li, C. A state-of-the-art review of crack branching. *Eng. Fract. Mech.* **257**, 108036 (2021).
- Yoon, J. et al. In situ tensile and fracture behavior of monolithic ultra-thin amorphous carbon in TEM. *Carbon* **196**, 236 (2022).
- Wagner, H. et al. Local elastic properties of a metallic glass. *Nat. Mater.* **10**, 439 (2011).
- Kapteijns, G., Richard, D., Bouchbinder, E. & Lerner, E. Elastic moduli fluctuations predict wave attenuation rates in glasses. *J. Chem. Phys.* **154**, 081101 (2021).

47. Sharon, E., Cohen, G. & Fineberg, J. Crack front waves and the dynamics of a rapidly moving crack. *Phys. Rev. Lett.* **88**, 085503 (2002).
48. Fineberg, J., Sharon, E. & Cohen, G. Crack front waves in dynamic fracture. *Int. J. Fract.* **121**, 55 (2003).
49. Adda-Bedia, M., Arias, R. E., Bouchbinder, E. & Katzav, E. Dynamic stability of crack fronts: out-of-plane corrugations. *Phys. Rev. Lett.* **110**, 014302 (2013).
50. Goldman Boué, T., Cohen, G. & Fineberg, J. Origin of the micro-branching instability in rapid cracks. *Phys. Rev. Lett.* **114**, 054301 (2015).
51. Lubomirsky, Y. & Bouchbinder, E. Facet formation in slow three-dimensional fracture. Preprint at <https://arxiv.org/abs/2403.17781> (2024).

Acknowledgements

This work has been supported by the United States-Israel Binational Science Foundation (BSF, grant no. 2018603, E.B.). E.B. acknowledges support from the Ben May Center for Chemical Theory and Computation, and the Harold Perlman Family. We thank Michael Zaiser and Shucheta Sheguftha, who reviewed this manuscript (together with two additional anonymous reviewers), for pushing us to study also 2D disordered materials.

Author contributions

Y.L. and E.B. designed the research, conceptualized the research and developed the theoretical picture. Y.L. developed the computational platform, performed all numerical simulations, analyzed them and generated all figures. E.B. wrote the manuscript with the help of Y.L.

Competing interests

The authors declare no competing interests.

Additional information

Supplementary information The online version contains supplementary material available at <https://doi.org/10.1038/s41467-024-51573-6>.

Correspondence and requests for materials should be addressed to Eran Bouchbinder.

Peer review information *Nature Communications* thanks Laurent Ponson and Michael Zaiser who co-reviewed with Shucheta Sheguftha, and the other anonymous reviewer(s) for their contribution to the peer review of this work. A peer review file is available.

Reprints and permissions information is available at <http://www.nature.com/reprints>

Publisher's note Springer Nature remains neutral with regard to jurisdictional claims in published maps and institutional affiliations.

Open Access This article is licensed under a Creative Commons Attribution-NonCommercial-NoDerivatives 4.0 International License, which permits any non-commercial use, sharing, distribution and reproduction in any medium or format, as long as you give appropriate credit to the original author(s) and the source, provide a link to the Creative Commons licence, and indicate if you modified the licensed material. You do not have permission under this licence to share adapted material derived from this article or parts of it. The images or other third party material in this article are included in the article's Creative Commons licence, unless indicated otherwise in a credit line to the material. If material is not included in the article's Creative Commons licence and your intended use is not permitted by statutory regulation or exceeds the permitted use, you will need to obtain permission directly from the copyright holder. To view a copy of this licence, visit <http://creativecommons.org/licenses/by-nc-nd/4.0/>.

© The Author(s) 2024